Pergamon

Int. J. Heat Mass Transfer. Vol. 38, No. 9, pp. 1553–1563, 1995

0017-9310/95 $9.50+0.00

0017-9310(94)00286-X

Macrosegregation near a cast surface caused by exudation and solidification shrinkage

EINAR HAUG, ASBJØRN MO† and HÅVARD J. THEVIK
SINTEF, Box 124 Blindern, 0314 Oslo, Norway

(*Received* 4 *May* 1994 *and in final form* 30 *August* 1994)

Abstract—A one-dimensional mathematical model for the development of an exudated layer and macrosegregation near a cast surface is established. While forced convection leads to a highly segregated layer at the surface of the casting and a solute depleted zone near the surface, solidification shrinkage induced flow makes the negative segregation within the casting less pronounced. Parameter studies reveal that the heat transfer coefficient for chill contact, the metallostatic head, and the criterion for onset of exudation, all have a major influence on the resulting macrosegregation. The mathematical model is used to estimate macrosegregation development in the direct chill casting of an Al–4.5% Cu rolling slab. It is found that both forced convection and shrinkage-induced flow have a significant effect on the macrosegregation near the cast surface.

1. INTRODUCTION

Macrosegregation formation close to and at the surface often reduces the quality of direct chill (DC) cast aluminium. Edge cracking during hot rolling of DC cast slabs is strongly related to the macrosegregation in the vicinity of the surface [1]. Furthermore, using ingots with pronounced macrosegregation near the surface for extrusion leads to large local variations in the extruded profiles.

Solidification gives rise to transport of interdendritic liquid in order to feed shrinkage. This leads to a solute-rich region near the chill surface commonly referred to as *inverse segregation*. Another mechanism behind macrosegregation close to the surface, which is particularly operative during aluminium DC casting, is related to air gaps between the semi-solid shell and the mould caused by solidification contraction. The metallostatic head will force the interdendritic liquid through the shell, past the original casting surface, and into the air gap. This flow phenomenon is referred to as *exudation* [2, p. 252]. The surface layer being formed by the exuding interdendritic liquid is highly enriched on alloying elements. While inverse segregation caused solely by solidification shrinkage is positive close the surface, the semi-solid shell through which exudation has taken place is depleted of alloying elements.

Several studies in which either inverse segregation or exudation have been treated separately have been carried out. Scheil [3] quantitatively described inverse segregation, and Kirkaldy and Youdelis [4] developed a one-dimensional macrosegregation model and measured inverse segregation in Al–Cu alloys. Flemings and Nereo [5] furthermore showed that the various types of macrosegregation can be quantitatively described by the same basic mechanism. Together with co-workers, Flemings *et al.* [6, 7] obtained a good agreement between predicted and measured inverse segregation for Al–Cu alloys. More recent measurements of inverse segregation can be found in refs. [8–10], and recent modelling studies can be found in refs. [11–14]. Work directed towards the exudation phenomenon can be found in refs. [15–20]. Mo *et al.* [21, 22] applied a one-dimensional model with a prescribed temperature field as input to predict the macrosegregation and surface layer due to exudation.

Kaempffer and Weinberg [23] performed an experiment in which macrosegregation was caused by both solidification shrinkage and exudation. However, to the knowledge of the authors, there exists no modelling studies quantifying macrosegregation close to a surface caused by the combined effect of solidification shrinkage and exudation. The purpose of the present work is therefore to model these two mechanisms simultaneously.

Based on the general volume averaging approach [24, 25], a simplified one-dimensional model for the solidification of a binary alloy is presented in Section 2. Section 3 is devoted to investigating how different casting parameters affect macrosegregation near a surface. Model predictions are furthermore compared with experimental results, and the model is applied in an example relevant to DC casting.

2. MATHEMATICAL MODEL

With reference to Fig. 1, a one-dimensional model describing the time evolution of solute concentration, temperature, liquid fraction, velocity and pressure along the x-axis is to be outlined. The solution domain

† Author to whom correspondence should be addressed.

NOMENCLATURE

c	solute concentration (mass fraction)
C	specific heat
d	secondary dendrite arm spacing
g	acceleration due to gravity; volume fraction (if subscript)
H	metallostatic head
k	partition coefficient
K	permeability
L	length of solution domain
m	slope of the liquidus line
M	function defining the mushy zone: $M(g_l) = 1$ for $0 < g_l < 1$; $M(g_l) = 0$ elsewhere
p	liquid pressure
S	interfacial area per solid volume
t	time
T	temperature
U	superficial velocity
V	casting velocity
x	position.

Greek symbols

α	heat transfer coefficient
β	solidification shrinkage factor ($\beta = \rho_s/\rho_l - 1$)
Δh	specific latent heat
Δr	thickness of exudated layer
λ	heat conductivity
μ	dynamic liquid viscosity
ρ	density.

Subscripts

0	surroundings
1	chill contact
2	no chill contact
e	eutectic
i	initial
l	liquid
m	melting point
prev	value from the previous iteration
s	solid.

Superscripts

*	quantity related to the change in boundary conditions at $x = 0$
ex	exudated.

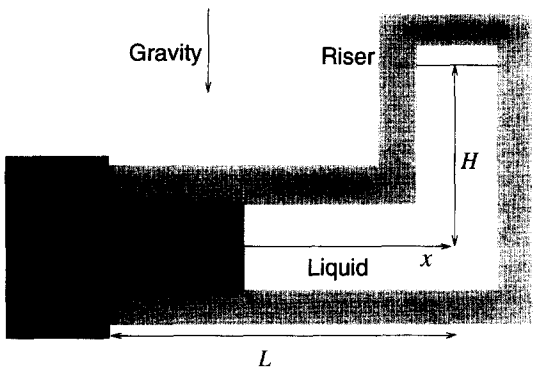

Fig. 1. The model problem.

is $0 \leqslant x \leqslant L$, and H is the height of the liquid in the riser. The riser itself is not a part of the solution domain.

The surface at $x = 0$ can either be in contact with the chill or there can be a situation in which the semi-solid shell has contracted from the chill. The heat flux at $x = 0$ is modelled by introducing an effective heat transfer coefficient which, during chill contact, is considerably higher than the coefficient in the situation of no chill contact. While chill contact implies that the liquid velocity is zero at $x = 0$, no contact is modelled by assuming that the pressure of the interdendritic melt at $x = 0$ is equal to the atmospheric pressure. The exudated layer which forms on the casting surface is usually very thin ($\sim 10^{-3}$ m). It is therefore not included in the solution domain.

At $x = L$, we assume that there is no heat flux caused by thermal diffusion. Due to shrinkage and exudation, mass (and energy) is transported from the riser into the solution domain. The velocity of the incoming liquid is implicitly given by the total mass feeding necessary to avoid pore formation (cf. assumption no. 6 below). The liquid which enters the solution domain has a temperature equal to the temperature at $x = L$. The liquid pressure at $x = L$ equals the atmospheric pressure plus the metallostatic head in the riser. Although the metallostatic head will decrease slightly due to solidification shrinkage and exudation in an experimental situation similar to that in Fig. 1, we regard H as a constant in the parameter studies in Section 3.1.

2.1. *Governing equations*

The model is based on the general volume averaged conservation equations summarized in ref. [25, Table 1], and the following simplifications and assumptions are imposed:

(1) All transport processes are one-dimensional and horizontal.

(2) The solid phase is stationary and rigid.

(3) Thermophysical properties are constant within each phase.

(4) The specific heat is equal in the solid and liquid phase.

(5) The momentum equation for the liquid phase is modelled by Darcy's law.

(6) There is no pore formation.

(7) There is no macroscopic diffusion of solute.

(8) The dispersion fluxes are neglected.

(9) The alloy is binary.

(10) There is local thermodynamical equilibrium in the mushy zone. The lever rule is applied.

(11) The liquidus and solidus in the phase diagram are straight lines.

The first of the above assumptions implies that naturally induced convection cannot be included in the model. The aluminium DC casting process is focused on in the present study, and we believe that solidification shrinkage induced flow and interdendritic flow associated with exudation are the main mechanisms behind the macrosegregation close to the DC cast surface. However, naturally induced convection can contribute to macrosegregation in central regions of the casting [2, p. 244–252], and we refer to refs. [26–34] for studies on macrosegregation caused by natural convection. Also assumption no. 6 is motivated by the aluminium DC casting application. In this process shrinkage cavities hardly appear due to adequate feeding. Furthermore, the low hydrogen content and the relatively rapid cooling lead to little pore formation [35]. Neglecting the macroscopic liquid solute diffusion (assumption no. 7), which typically is 10^4 larger than solute diffusion in the solid phase, is motivated from the results in ref. [12], in which nearly identical inverse segregation profiles were obtained with and without solute diffusion in the liquid.

Adding the mass conservation equations for the solid and liquid phases yields

$$\frac{\partial \rho}{\partial t} + \frac{\partial}{\partial x}(\rho_l U_l) = 0 \tag{1}$$

where $\rho = g_l\rho_l + g_s\rho_s$ is the density of the two-phase averaging volume, and g_l, ρ_l and g_s, ρ_s are the volume fraction and density of the liquid and solid phases, respectively. U_l is the superficial liquid velocity and t is the time. It is seen from equation (1) that $\rho_l \neq \rho_s$ gives rise to a non-zero liquid velocity. Proper modelling of the densities, which depend on solute concentration and temperature, is therefore expected to be crucial. However, Flemings *et al.* [6] showed that constant densities yield essentially the same shrinkage-induced velocity as if the densities were modelled as functions of solute concentration and temperature. Hence, we assume the densities to be constant and introduce the solidification shrinkage factor defined according to $\beta = \rho_s/\rho_l - 1$. The mass conservation can then be rewritten in the form

$$\beta \frac{\partial g_l}{\partial t} = \frac{\partial U_l}{\partial x}. \tag{2}$$

Momentum conservation for the liquid phase in the mushy zone is modelled by

$$\frac{\mu}{K} U_l + \frac{\partial p}{\partial x} = 0 \tag{3}$$

where μ, K and p are the dynamic viscosity, the permeability of the dendritic network, and the pressure, respectively. In the present work, the Kozeny–Carman relation is employed for the permeability, i.e.

$$K = \frac{g_l^3}{5S^2(1-g_l)^2} \tag{4}$$

where S is the solid–liquid interface area per solid volume. Following Asai and Muchi [27], we assume that $S = 6/d$, where d is the secondary dendrite arm spacing. The melt in the pure liquid zone is modelled as an ideal fluid with negligible inertial forces, implying $\partial p/\partial x = 0$. This corresponds to the limiting form of equation (3) for $g_l = 1$ ($K \to \infty$ when $g_l \to 1$). Because the solid phase is assumed to be stationary and rigid, only the momentum conservation of the liquid phase needs to be considered.

Energy conservation can be expressed in terms of the temperature by

$$\rho C \frac{\partial T}{\partial t} + \rho_l C U_l \frac{\partial T}{\partial x} = \frac{\partial}{\partial x}\left[(g_l\lambda_l + g_s\lambda_s)\frac{\partial T}{\partial x}\right] - \rho_s \Delta h \frac{\partial g_l}{\partial t} \tag{5}$$

where C, T, λ_l, λ_s and Δh are the specific heat, the temperature, the heat conductivities in the liquid and solid phases, and the latent heat, respectively.

By adding the solute conservation equations for the liquid and solid phases, we obtain

$$\frac{\partial}{\partial t}(\rho c) + \rho_l \frac{\partial}{\partial x}(c_l U_l) = 0 \tag{6}$$

where $c = (g_l\rho_l c_l + g_s\rho_s c_s)/\rho$ is the total solute concentration, and c_l and c_s are the solute concentrations in the liquid and solid phases, respectively.

Solidification is modelled by the lever rule. Since g_l equals zero below the solidus line and one above the liquidus line, we can express the assumption of local thermodynamical equilibrium by

$$g_l(c, T) = \begin{cases} 0 & \text{if } c \leqslant kc_l(T) \\ \dfrac{\rho_s(c - kc_l(T))}{c(\rho_s - \rho_l) + c_l(T)(\rho_l - k\rho_s)} & \text{if } kc_l(T) < c < c_l(T) \\ 1 & \text{if } c_l(T) \leqslant c \end{cases} \tag{7}$$

$k = c_s/c_l$ is the partition coefficient, and $c_l(T)$ is given by

$$c_l(T) = (T - T_m)/m \tag{8}$$

where T_m is the melting point of the pure metal and m is the slope of the liquidus line. Since g_l is zero below the eutectic temperature T_e, relation (7) applies when the total concentration is less than $kc_l(T_e)$.

The physics of the boundaries have been discussed above, and can be formulated mathematically as

$x = 0$:

$$\begin{cases} U_l = 0 & (g_l\lambda_l + g_s\lambda_s)\dfrac{\partial T}{\partial x} = \alpha_1(T - T_0) \\ & \text{if chill contact} \\ p = p_0 & (g_l\lambda_l + g_s\lambda_s)\dfrac{\partial T}{\partial x} = \alpha_2(T - T_0) \\ & \text{if no chill contact} \end{cases} \tag{9}$$

$$x = L: \quad p = p_0 + \rho_l g H \quad \frac{\partial T}{\partial x} = 0. \tag{10}$$

Here, α_1 and α_2 are the heat transfer coefficients corresponding to chill contact and no chill contact, respectively. T_0, p_0 and g are the temperature of the surroundings at $x = 0$, the atmospheric pressure, and the gravity constant, respectively.

The initial conditions are a uniform temperature field ($T = T_i$), liquid only ($g_l = 1$), a uniform concentration ($c = c_i$), and no liquid velocity ($U_l = 0$).

Except for the momentum equation, which is not valid in the solid region, the governing equations are valid in the pure liquid, mushy and pure solid zones. When $g_l = 1$, U_l is constant, $p = p(x = L)$, and since the liquid–mush interface moves from the left to the right in all the below case studies, it follows that $c = c_i$. In the pure solid zone, $U_l = 0$ and c is constant. Hence, only the temperature equation is to be solved everywhere in the solution domain, $0 \leqslant x \leqslant L$.

Quantities characterizing the exudation are the layer thickness, Δr, and the average solute concentration in the layer, c^{ex}. These quantities are calculated by the relations

$$\Delta r = -\int_0^t U_l(x = 0, t)\,\mathrm{d}t \tag{11}$$

$$c^{ex} = -\frac{1}{\Delta r}\int_0^t c_l(x = 0, t)U_l(x = 0, t)\,\mathrm{d}t. \tag{12}$$

2.2. *Solution procedure*

When there is chill contact, the velocity of the one-dimensional problem is determined solely from the mass continuity equation (2), since no pressure boundary conditions are then to be imposed. In the case of no chill contact we combine equations (2) and (3) and obtain a pressure equation of the form

$$\frac{\partial}{\partial x}\left(K\frac{\partial p}{\partial x}\right) = -\mu\beta\frac{\partial g_l}{\partial t} \tag{13}$$

which is to be solved in the mushy zone.

It turned out that treating the latent heat term in equation (5) as a source term resulted in convergence problems. We therefore combine equations (2), (6) and (8) along with $c_s = kc_l$, and obtain for $0 < g_l < 1$

$$[(1-k(1+\beta))T-(1+\beta)(1-k)T_m]\frac{\partial g_l}{\partial t} = -[g_l+k(1+\beta)(1-g_l)]\frac{\partial T}{\partial t} - \frac{\partial}{\partial x}(U_l T) \tag{14}$$

by which the time derivative of g_l in the mushy zone is related to the time derivative of T. Inserting this equation into the energy equation (5) yields the following temperature equation:

$$C\frac{\partial}{\partial t}(\rho T) - \frac{M(g_l)\rho_s\Delta h[g_l+k(1+\beta)(1-g_l)]}{(1-k(1+\beta))T-(1+\beta)(1-k)T_m}\frac{\partial T}{\partial t} + \left[\rho_l C - \frac{M(g_l)\rho_s\Delta h}{(1-k(1+\beta))T-(1+\beta)(1-k)T_m}\right] \times \frac{\partial}{\partial x}(U_l T) = \frac{\partial}{\partial x}\left[(g_l\lambda_l + g_s\lambda_s)\frac{\partial T}{\partial x}\right] \tag{15}$$

where $M(g_l)$ is equal to one in the mushy zone and zero elsewhere. $M(g_l)$ ensures the validity of equation (15) everywhere.

Equations (2), (3), (6), (13) and (15) have been discretized by an implicit control-volume-based finite difference procedure. The resulting set of difference equations has been solved sequentially, and the implicit solution has been obtained by iterating on each time step. The solution procedure at any new time step is:

(1) T is updated by equation (15), in which the previous values for g_l and U_l are inserted. The equation is linearized by applying the previous value of T in the coefficients.

(2) g_l is updated from equations (7) and (8) in which T from step 1 and the previous value for c are inserted.

(3) U_l is updated by solving equation (2) in the case of chill contact. When there is no chill contact, we solve equation (13) for p and then equation (3) for U_l. In either case we use g_l from step 2.

(4) In order to update the total solute concentration c, we use equation (6) with equation (8) inserted. Here we use T from step 1, g_l from step 2 and U_l from step 3.

These four steps are repeated until

$$\frac{\max(|T - T_{prev}|)}{\max T} + \frac{\max(|c - c_{prev}|)}{\max c} + \frac{\max(|g_l - g_{l,prev}|)}{\max g_l} \leqslant 10^{-3}. \tag{16}$$

Depending on how fast (slow) the above iteration procedure converges, the time step size is increased (decreased). A small step size is typically needed when solidification starts or when the boundary conditions are changed. 200 grid points have been used in the parameter studies in Section 3.1. Conservation of total mass, species mass and enthalpy has been checked, and the relative error in these global quantities is less than 0.01%.

Table 1. Thermophysical data for Al–4.5% Cu and casting conditions in the reference case

Symbol	Value	Reference
C†	1060 J kg^{-1} K^{-1}	[38]
d	40 μm	
k	0.17	[39]
m	−339 K	[39]
T_e	821 K	[39]
T_m	933 K	[39]
β‡	0.065	[40]
Δh	400×10^3 J kg^{-1}	[38]
λ_l	83 W m^{-1} K^{-1}	[38]
λ_s	192 W m^{-1} K^{-1}	[38]
μ	3×10^{-3} kg m^{-1} s^{-1}	[38]
ρ_l§	2480 kg m^{-3}	[40, 41]
ρ_s§	2641 kg m^{-3}	
c_l	4.5%	
g_l*	0.19	[22]
H	0.08 m	
L	0.2 m	
T_0	293 K	
T_i	973 K	
α_1	1000 W m^{-2} K^{-1}	
α_2	300 W m^{-2} K^{-1}	

† Cf. assumption no. 4 in Section 2.1.
‡ β has the value for *pure* aluminium.
§ ρ_l corresponds to a copper concentration of 4.5% at 933 K. ρ_s is defined as $\rho_s = (1+\beta)\rho_l$.

The solution algorithm has been implemented in MATLAB [36], and the CPU time for each of the modelling cases in Section 3.1 is less than 1 h on a Hewlett–Packard-9000s735 workstation.

3. RESULTS AND DISCUSSION

3.1. *Parameter studies*

Reference case. The modelling example referred to as the reference case is defined as follows. For $0 \leqslant t \leqslant t^*$ the liquid–mush is in contact with the chill, and at $t = t^*$ the chill is removed allowing exudation to occur for $t > t^*$. t^* is the time when the liquid fraction at $x = 0.45$ cm becomes less than some critical value g_l^* for the first time. This criterion for change in the boundary conditions corresponds to that used for air gap formation in studies of the DC casting process [15, 22, 37]. As in ref. [22], we have chosen g_l^* to be 0.19, which leads to $t^* = 30.4$ s. The calculation is terminated when the solid–mush interface reaches $x = 8$ cm. The alloy is Al–4.5% Cu and thermophysical data is displayed in Table 1 along with the casting conditions.

Curve 1 in Fig. 2 represents the inverse segregation situation at $t = 30$ s just before exudation starts. Curves 2 and 3 in Fig. 2 for $t = 50$ and 100 s, respectively, show that the flow driven by the metallostatic head leads to a decrease in the positive segregation close to the surface as well as a further solute depletion in the already negative segregated part of the mushy zone. There is a clear minimum in the final solute content (curve 4) at $x \approx 1$ cm. Figure 2 furthermore reveals that the final solute concentration is higher

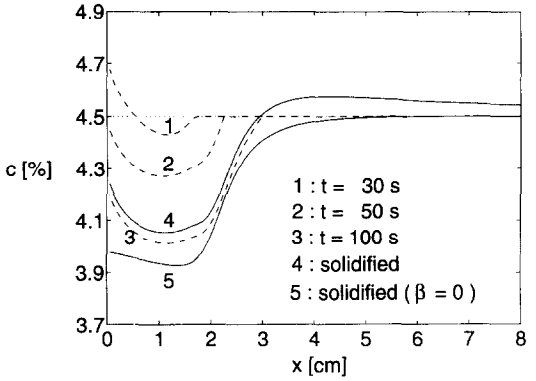

Fig. 2. Evolution of the solute concentration distribution in the reference case. The final distribution when solidification shrinkage is neglected ($\beta = 0$), is also shown.

than the solute concentration at 100 s (curve 3). The reason for this is that the shrinkage-induced flow is larger than the flow caused by the metallostatic head during the last stage of solidification. The forced convection through the mushy zone is then small because g_l has a low value. On the other hand, flow due to solidification shrinkage does not depend on the actual value of the liquid fraction, but on the rate of change of g_l [cf. equation (2)].

Figure 3(b) displays the time evolution of the thickness of the exudated layer Δr. The main contribution to Δr comes in the time interval $30 \lesssim t \lesssim 150$ s. This is related to the decreased heat transfer coefficient, which leads to reheating near the surface [cf. Fig. 3(a)]. At $x = 0$, the liquid fraction increases from 0.12 at $t = t^*$ to 0.25 at $t \approx 50$ s (see curve 3 in Fig. 5). It then follows from the Kozeny–Carman relation (4) that the permeability increases by a factor 12. For $150 \lesssim t \lesssim 300$ s, the liquid fraction becomes smaller, and the velocity at $x = 0$ approaches zero. Since the forced convection is negligible when $300 \lesssim t \lesssim 550$ s and solidification still induces a flow in order to avoid pore formation, mass is transported from the surface and into the mushy zone. This *positive* velocity at $x = 0$ is very small, and it leads to the small decrease in Δr seen in Fig. 3(b). For $t \gtrsim 550$ s g_l is zero at $x = 0$ and Δr does not change.

It is seen from Fig. 3(c) that the average solute concentration in the exudated layer c^{ex}, decreases strongly in the first 20 s during exudation and then increases slightly. From equation (12) it follows that changes in the temperature at the surface are reflected in c^{ex} since c_l is a function of the temperature. The change in thermal boundary conditions leads to a temperature increase at the surface of more than 20 K [cf. Fig. 3(a)], which implies the decreasing c^{ex}. The surface temperature decreases when $t \gtrsim 70$ s, which results in the increase in c^{ex}.

It should be noted that the macrosegregation influences the liquid fraction due to so-called constitutional solidification (or remelting). For example when $T = 890$ K, a solute concentration of 4.5% cor-

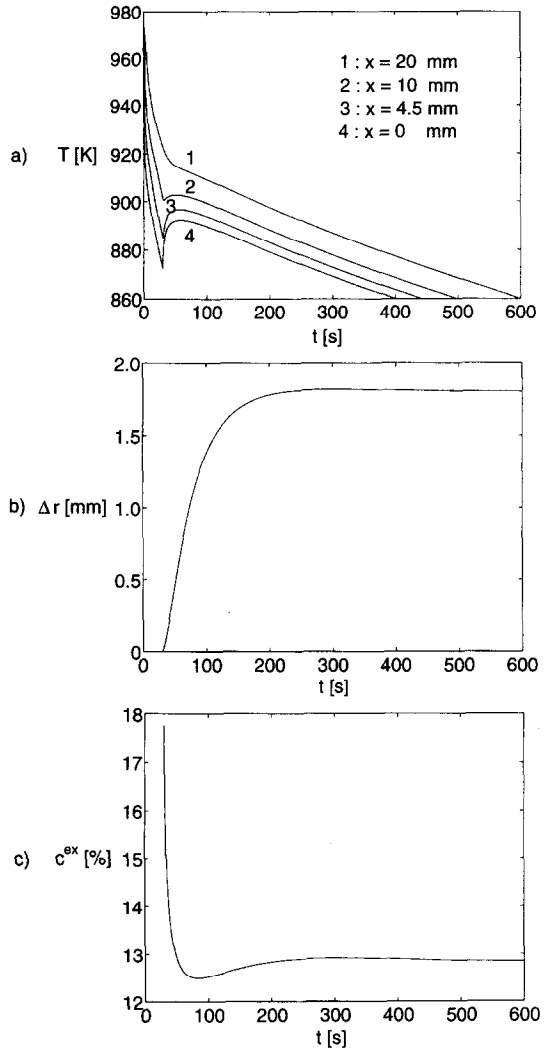

Fig. 3. Time evolution in the reference case: (a) temperature at four x-positions; (b) thickness of the exudated layer; (c) average solute concentration in the exudated layer.

responds to a g_l-value of 0.23, while it is 0.19 for $c = 4.1\%$. Severe exudation therefore leads to a decrease in the liquid fraction, which in turn leads to reduced exudation.

Exudation only. Only the metallostatic head was considered as the driving force for the interdendritic flow in refs. [21, 22]. This corresponds to setting $\beta = 0$ in the present model and leads to the final macrosegregation represented by curve 5 in Fig. 2. Comparing curve 5 with curve 4 (which is the final macrosegregation in the reference case) reveals that the solidification shrinkage-induced flow decreases the solute depletion caused by the forced convection.

Even though there is no shrinkage effect tending to increase the solute content near the surface when $\beta = 0$, there is also in curve 5 (as in the other curves in Fig. 2) a minimum in the solute concentration at some distance from the chill. In order to explain this, we combine equations (2), (6) and (8) and obtain for $\beta = 0$

Table 2. Data for the exudated layer

Case study	Δr [mm]	c^{ex} [% Cu]
Reference case	1.8	12.9
Exudation only, $\beta = 0$	1.7	12.7
$\alpha_l = 300$ W m^{-2} K^{-1}	0.20	16.3
$\alpha_l = 600$ W m^{-2} K^{-1}	0.89	14.6
$H = 0.05$ m	1.2	13.0
$H = 0.11$ m	2.3	12.7
$g_l^* = 0.09$	0.56	15.7
$g_l^* = 0.24$	2.6	11.7
DC casting case, $\beta = 0.065$	0.75	15.2
DC casting case, $\beta = 0$	0.73	14.8

$$\frac{\partial}{\partial t}(\rho c) = -\frac{\rho_l}{m} U_l \frac{\partial T}{\partial x} \tag{17}$$

from which we see that $\partial/\partial t(\rho c)$ is proportional to the superficial velocity times the temperature gradient. $\partial T/\partial x$ is largest close to the surface, except when remelting occurs, as revealed by the distance between the temperature curves in Fig. 3(a). The minimum in curve 5 is therefore a result of a maximum in $\partial T/\partial x$ at some distance from the chill combined with a relatively large velocity U_l during the period of remelting.

While the thickness of the exudated layer is 1.8 mm in the reference case, it is 1.7 mm when $\beta = 0$. This indicates that the exudation is mainly due to the flow driven by the metallostatic head. The 0.1 mm thinner layer for $\beta = 0$ is a result of the lower solute concentration for $\beta = 0$, which leads to a lower liquid fraction, and thereby lower permeability.

The heat transfer coefficient. The heat transfer coefficient has a pronounced influence on the exudation and macrosegregation. As summarized in Table 2, $\alpha_l = 600$ and 300 W m^{-2} K^{-1} reduce the layer thickness by approximately 50% and 90%, respectively, compared with the reference case. When $\alpha_l = 300$ W m^{-2} K^{-1}, curves 1 and 2 in Fig. 4 furthermore reveal that the final macrosegregation becomes almost equal to the inverse segregation profile, this being the result if no exudation were present. These

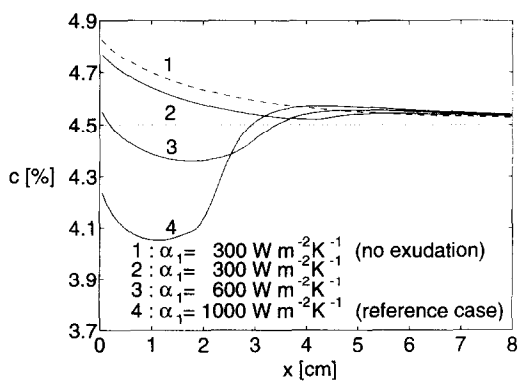

Fig. 4. The final solute distribution for different choices of the heat transfer coefficient during chill contact. Also the inverse segregation profile obtained for $\alpha_l = 300$ W m^{-2} K^{-1}, when there is no exudation, is shown.

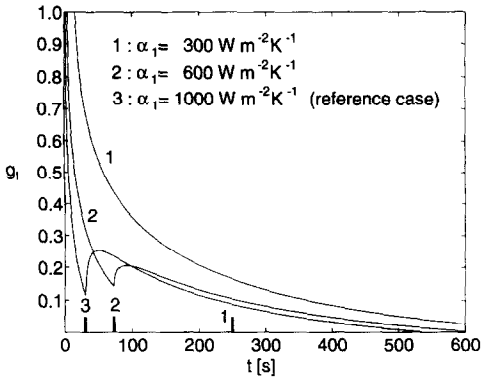

Fig. 5. The liquid fraction at $x = 0$ for different choices of α_l. The thick labels at the time axis indicate the time at which exudation starts for each choice of α_l.

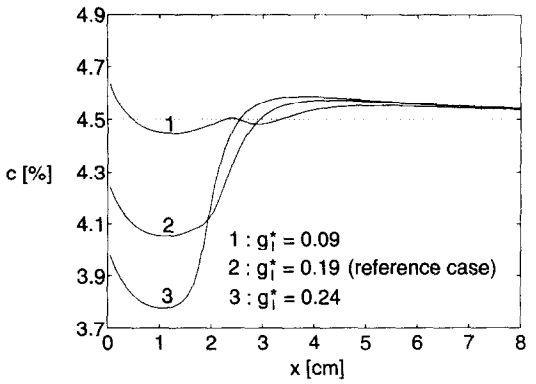

Fig. 7. The final solute distribution for different choices of the parameter g_l^* in the criterion for air gap formation.

results are due to the reduced remelting when α_l is reduced, as shown in Fig. 5. Since the permeability is very sensitive to changes in g_l at low liquid fractions, the relatively small differences in liquid fraction corresponding to the different values of α_l lead to considerable differences in the permeability, and thereby differences in the thickness of the exudated layer and the final solute distribution.

The results in Table 2 indicate that c^{ex} increases with decreasing α_l. Even though the surface temperature and thereby the concentration of the exuding melt is approximately the same when exudation starts, there is less reheating for $\alpha_l = 600$ and 300 W m^{-2} K^{-1} compared with the reference case and consequently less exudation at higher temperatures. Hence, the material exuded at lower temperatures is weighted more in the calculation of the average solute concentration.

Metallostatic head. The effect of varying the metallostatic head H is summarized in Table 2 and Fig. 6. It is seen that Δr and the solute depletion increase with the metallostatic head, since H is proportional to the driving force for exudation. Because c^{ex} is related to the temperature at which exudation occurs and because this temperature is nearly independent of the metallostatic head, the solute concentration in the exudated layer is nearly independent of H.

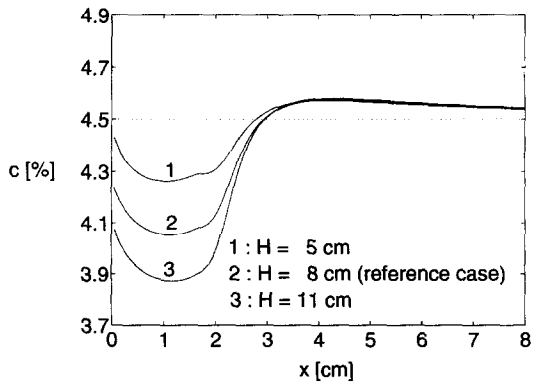

Fig. 6. The final solute distribution for different choices of the metallostatic head H.

It can be seen from the governing equations that H has the same influence on the solution as the square of the secondary dendrite spacing, d. Figure 6 therefore reveals that the final solute distribution is strongly dependent on the characteristic microscopic length d.

Mushy shell thickness. In the criterion for the formation of an air gap between the casting and the chill we have followed refs. [15, 22, 37]. When the liquid fraction at $x = 0.45$ cm exceeds the critical value g_l^*, we assume the mushy shell to be thick enough for an air gap to form. The thickness of the mushy shell when exudation starts strongly affects the final macrosegregation. We have therefore in Fig. 7 displayed the final solute distribution for g_l^* equal to 0.09, 0.19 (reference case) and 0.24. We see that an increase in g_l^* leads to a more pronounced negative segregated zone, which reflects the decrease in the value of t^* when exudation starts. We furthermore note from the results in Table 2 that an increased g_l^* corresponds to a thicker exudated layer.

It can be seen that curve 1 in Fig. 7 exhibits a local maximum at $x \approx 2.3$ cm when $g_l^* = 0.09$. The position of this concentration peak corresponds to the position of the liquid–mush interface at $t = t^*$. As pointed out in a study of segregated bands by Diao and Tsai [14], the peak reflects the increase in shrinkage-induced flow due to the reduction in heat transfer coefficient and solidification rate. The local maximum is most clearly seen for low g_l^*-values because flow associated with exudation then is small. A similar peak can be seen in curve 1 in Fig. 6, representing the lowest metallostatic head.

3.2. *Comparison with experiments*

Our model predictions are qualitatively in correspondance with Kaempffer and Weinberg's [23] experimental results. Both a segregation profile with a clear minimum at some distance from the chill and a highly enriched exudated layer were measured in these experiments on a Cu–8% Ag alloy. However, in an attempt to model these experiments quantitatively,

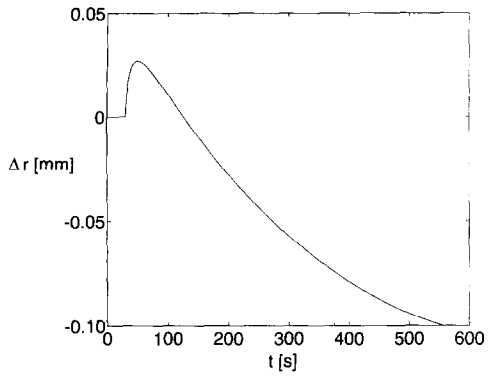

Fig. 8. The thickness of the exudated layer as a function of time when the metallostatic head is zero. Otherwise the casting conditions are the same as in the reference case.

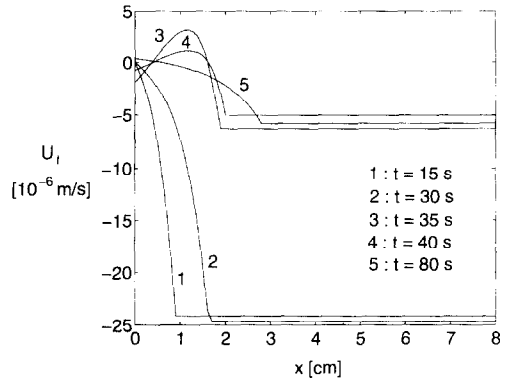

Fig. 9. The velocity distributions at five different times when the metallostatic head is zero. Otherwise the casting conditions are the same as in the reference case.

we were not able to reproduce the experimental temperature histories. We believe this discrepancy to be a result of our simplified, one-dimensional model concept. There furthermore seems to have been some uncertainty in the position at which the temperature was logged.

Ohm and Engler [20] have reported experiments similar to those in ref. [23]. More specifically, they qualitatively observed that the exudation due to remelting and the associated volume expansion of the mushy shell is considerably less than the exudation due to forced convection driven by metallostatic head. In their experiment, exudation associated with the metallostatic head was suppressed by balancing the metallostatic head with a gas pressure at the surface of the casting. In order to isolate the effect of partial remelting of the mushy shell in our model, we have set $H = 0$ and otherwise used the same data as in the reference case.† The time development of Δr for this case is shown in Fig. 8. It is seen that the expansion of the semi-solid shell associated with the remelting leads to a maximum in Δr of approximately 0.03 mm at $t \approx 50$ s. In accordance with the experimental results in ref. [20], this value of Δr is very small compared to the thickness of the exudated layer in the reference case (1.8 mm). The time evolution of Δr can be explained by considering Fig. 9, in which the velocity distributions at five different times are displayed. Curves 1 and 2 represent the classical inverse segregation case at 15 and 30 s, respectively. At 35 and 40 s (curves 3 and 4, respectively), the remelting leads to a negative velocity at the surface and the exuded layer increases. After the remelting ends at $t \approx 50$ s, the solidification shrinkage gives rise to a positive velocity at $x = 0$ (curve 5), which in turn leads to the decrease in Δr seen in Fig. 8. The fact that Δr becomes negative indicates that solidification shrinkage alone does not lead to any net exudation on the resulting casting.

There is a fairly good agreement between Flemings and Nereo's [7] measured inverse segregation (no exudation present) and predictions obtained by our model. This is revealed in Fig. 10, and it might be of interest to note that our simplified model yields results which fit the experimental results in ref. [7] almost equally as well as the more elaborate two-dimensional model predictions carried out by Diao and Tsai [12]. We refer here to Fig. 12 in ref. [12], in which the solidification shrinkage factor was chosen as high as 0.104. Diao and Tsai [12] furthermore reported simulation times of about 100 h CPU, whereas solving the equations in the present model requires less than 1 h CPU (on a comparable workstation).

3.3. *DC casting relevant example*

We finally apply the model for making an estimate of the exudation and macrosegregation development close to the surface during the DC casting of an Al–4.5% Cu rolling slab. In accordance with ref. [22], we neglect all transport processes which are not perpendicular to the casting surface, and, as indicated in

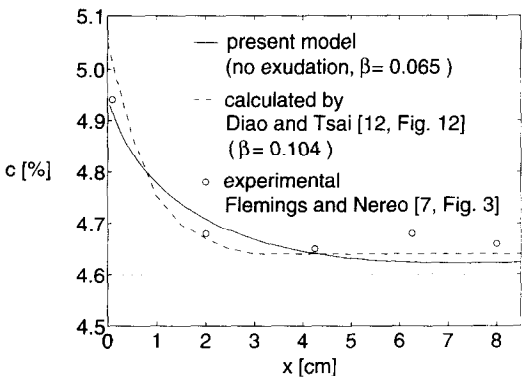

Fig. 10. Inverse segregation predicted by the model when $\alpha_l = 400$ W m^{-2} K^{-1}. Experimental results reproduced from ref. [7, Fig. 3] and model predictions reproduced from ref. [12, Fig. 12] in which $\beta = 0.104$, are also shown. The nominal solute concentration is 4.6%.

† Although the effective metallostatic head is zero ($H = 0$), the experimental situation of a 10 cm metallostatic head being balanced by a gas pressure implies that the model assumption of no pore formation is sound.

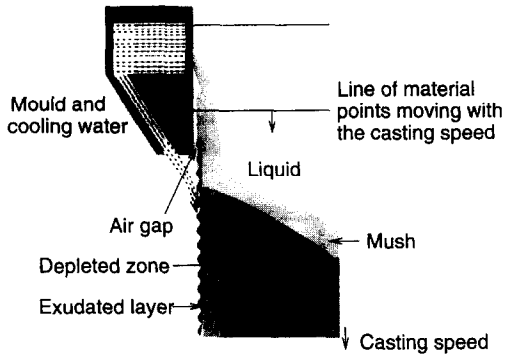

Fig. 11. The region near the mould in the DC casting process. The line of material points moving with the casting speed represents the solution domain $0 \leqslant x \leqslant L$ in the case study in Section 3.3.

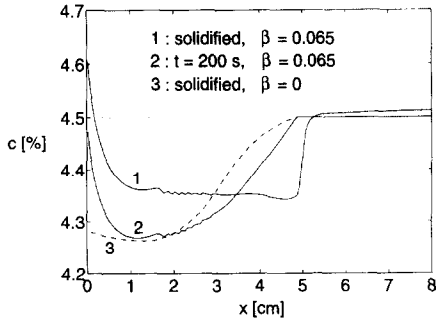

Fig. 13. Solute distribution after complete solidification and just before the direct water cooling impingement in the DC casting example. Also the macrosegregation obtained when the solidification shrinkage has been neglected ($\beta = 0$) is shown.

Fig. 11, follow a horizontal line of material points moving with the casting speed V equal to 0.75×10^{-3} m s^{-1}. This line represents the solution domain $0 \leqslant x \leqslant L$. The position $x = 0$ is situated at the casting surface, and $x = L$ corresponds to the centre of the casting.

The condition for the formation of an air gap is the same as in the reference case. However, because the mushy shell thickness will decrease during remelting, mould contact is restored if the semi-solid shell cannot withstand the metallostatic pressure acting on it. We address this mechanism as in refs. [15, 22, 37], and assume restored contact when g_l at $x = 0$ exceeds $g_l^* = 0.19$. The heat transfer coefficients α_1 and α_2 corresponding to mould contact and air gap, respectively, have the same values as in the reference case, and α_2 is increased linearly to 15000 W m^{-2} K^{-1} from 200 to 230 s in order to accommodate the direct water impingement below the mould. Assuming the line of material points to start at the top of the liquid pool at $t = 0$, the metallostatic head is Vt at $x = L$, reflecting that the material line moves downwards. Otherwise, the boundary and initial conditions are as described in Section 2, and thermophysical data and L are the same as in the reference case (cf. Table 1).

Figure 12 shows the temperature development in some chosen positions. The oscillatory temperature development reflects the repeated formation of air gaps and mould contact in correspondence with the temperature modelling results in ref. [15]. Contact with the mould is not restored anymore for $t \gtrsim 75$ s, since the solidifying alloy then no longer possesses enough energy to remelt.

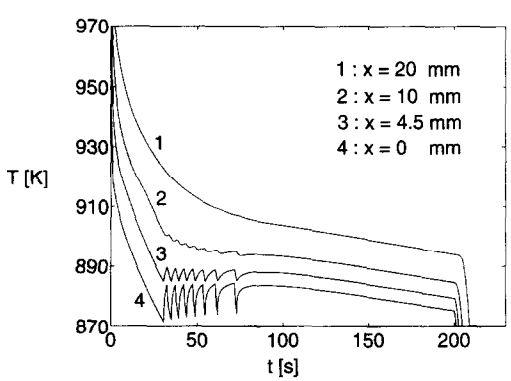

Fig. 12. Temperature as a function of time in four x-positions in the DC casting example. Direct water impingement starts at $t = 200$ s.

The solute distribution just before the direct water impingement ($t = 200$ s) and the final macrosegregation are displayed in Fig. 13. We see that the solidification shrinkage induced flow caused by the water cooling reduces the negative segregation and makes the depleted zone larger. The small spatial variations in curves 1 and 2 in Fig. 13 are a result of the oscillatory boundary conditions at $x = 0$.

Table 2 displays data related to the exudated layer, and it is seen that Δr after complete solidification is 0.75 mm, which corresponds to observations on real castings. The final value of c^{ex} is 15.2% Cu.

In their study of exudation in the DC casting process, Mo *et al.* [21, 22] neglected flow due to shrinkage. In Fig. 13 and Table 2 we have therefore included the final solute distribution, and the thickness and the concentration of the exudated layer, respectively, for a case study in which $\beta = 0$ (the other modelling parameters correspond to those above). While the shrinkage has very little influence on Δr and c^{ex}, we see that the difference in solute concentration within the casting is significant. The solidification shrinkage-induced flow can in other words have a pronounced influence on the macrosegregation close to the surface even in cases where the exudation is severe.

4. CONCLUSION

Macrosegregation development in an Al–4.5% Cu alloy caused by the combined effect of solidification shrinkage and exudation has been studied by means of a one-dimensional mathematical model.

- While exudation leads to a thin, solute rich surface layer and a negative segregated zone close to the casting surface, it has been shown that the solidification shrinkage makes the negative segregated

zone less pronounced. The thickness and the concentration of the exudated layer are, however, mainly due to the flow associated with the metallostatic head.

- A minimum in the solute concentration at some distance (~ 1 cm) from the cast surface has been predicted.
- The exudation and associated macrosegregation become less severe when the difference between the heat transfer coefficient for chill contact and for air gap is reduced. Also the metallostatic head, the characteristic microscopic length scale, and the criterion for formation of an air gap have a significant influence on the final solute distribution.
- In a modelling example relevant to DC casting of rolling slabs, it has been found that both shrinkage-induced flow and forced convection have a significant influence on the macrosegregation close to the casting surface.

Acknowledgement—This research was supported by The Norwegian Research Council through program No. STP.29643 : Simulation of Multiphase Flow. Professor Aslak Tveito and Professor Ragnar Winther are acknowledged for important input on the numerical part of the work. The authors thank Per Kolby for proof-reading the manuscript.

REFERENCES

1. I. H. Hove, B. Andersson, and D. Voss, Edge cracking during hot rolling of A15Mg. In *Proceedings of the 3rd Conference on Aluminium Alloys—Their Physical and Mechanical Properties* (Edited by L. Arnberg, O. Lohne, E. Nes and N. Ryum), Vol. 2, pp. 264–269, Trondheim (1992).
2. M. C. Flemings. *Solidification Processing*. McGraw-Hill, New York (1974).
3. E. Scheil. Beitrag zum problem der blockseigerung, *Metallforschung* **2,** 69–75 (1947).
4. J. Kirkaldy and W. V. Youdelis, Contribution to the theory of inverse segregation, *Trans. AIME* **212,** 833–840 (1958).
5. M. C. Flemings and G. E. Nereo, Macrosegregation, Part I. *Trans. Metall. Soc. AIME* **239,** 1449–1461 (1967).
6. M. C. Flemings, R. Mehrabian and G. E. Nereo, Macrosegregation, Part II, *Trans. Metall. Soc. AIME* **242,** 41–49 (1968).
7. M. C. Flemings and G. E. Nereo, Macrosegregation, Part III, *Trans. Metall. Soc. AIME* **242,** 50–55 (1968).
8. B. Prabhakar and F. Weinberg, Inverse segregation in Al–10 pct Cu, *Metall. Trans.* **9B,** 150–151 (1978).
9. T. Motegi and A. Ohno, Inverse segregation in unidirectionally solidified Al–Cu alloy ingots, *Trans. Jap. Inst. Metals* **25**(2), 122–132 (1984).
10. H. Kato and J. R. Cahoon, Inverse segregation in directionally solidified Al–Cu–Ti alloys with equiaxed grains, *Metall. Trans.* **16A,** 579–587 (1985).
11. S. Minakawa, I. V. Samarasekera and F. Weinberg, Inverse segregation, *Metall. Trans.* **16B,** 595–604 (1985).
12. Q. Z. Diao and H. L. Tsai, Modelling of solute redistribution in the mushy zone during solidification of aluminium–copper alloys, *Metall. Trans.* **24A,** 963–973 (1993).
13. J. H. Chen and H. L. Tsai, Inverse segregation for a unidirectional solidification of aluminium–copper alloys, *Int J. Heat Mass Transfer* **36**(12), 3069–3075 (1993).
14. Q. Z. Diao and H. L. Tsai, The formation of negative- and positive-segregated bands during solidification of aluminum–copper alloys, *Int J. Heat Mass Transfer* **36,** 4299–4305 (1993).
15. B. R. Henriksen and E. K. Jensen, Modelling the effect of casting speed and metal level on the surface segregation of AA5182. In *Light Metals*. TMS–AIME, Warrendale, PA (1993).
16. H. Kästner, Die umgekehrte Blockseigrung bei Strangguß I, *Z. Metall.* **41,** 193–205 (1950).
17. H. Kästner, Die umgekehrte Blockseigrung bei Strangguß II, *Z. Metall.* **41,** 247–254 (1950).
18. K. Buxmann, Mechanismen der Oberflächenseigrung von Strangguß, *Metall.* **31,** 163–170 (1977).
19. R. Ellerbrok and S. Engler, Untersucherungen zur Oberflächenseigrung von Stranggußlegierungen, *Metall.* **37,** 784–788 (1983).
20. L. Ohm and S. Engler, Treibende Kräfte der Oberflächenseigrungen beim NE-Strangguß, *Metall.* **43,** 520–524 (1989).
21. A. Mo, Mathematical modelling of surface segregation in aluminum DC casting caused by exudation, *Int J. Heat Mass Transfer* **36,** 4335–4340 (1993).
22. A. Mo, T. E. Johnsen, B. R. Henriksen, E. K. Jensen and O. R. Myhr, Modelling the surface segregation development in DC casting. In *Light Metals* (Edited by U. Mannweiler), pp. 889–896. TMS–AIME, Warrendale, PA (1994).
23. F. Kaempffer and F. Weinberg, Macrosegregation in a copper alloy directionally cast with exudation of liquid, *Metall. Trans.* **2,** 2477–2483 (1971).
24. S. Ganesan and D. R. Poirier, Conservation of mass and momentum for the flow of interdendritic liquid during solidification, *Metall. Trans.* **21B,** 173–181 (1990).
25. J. Ni and C. Beckermann, A volume-averaged two-phase model for transport phenomena during solidification, *Metall. Trans.* **22B,** 349–361 (1991).
26. R. Mehrabian, M. Keane and M. C. Flemings, Interdendritic fluid flow and macrosegregation. Influence of gravity, *Metall. Trans.* **1,** 1209–1220 (1970).
27. S. Asai and I. Muchi, Theoretical analysis and model experiments on the formation mechanism of channel-type segregation, *Trans. Iron Steel Inst. Jap.* **18,** 90–98 (1978).
28. W. D. Bennon and F. P. Incropera, A continuum model for momentum, heat and species transport in binary solid–liquid phase change systems—II. Application to solidification in a rectangular cavity, *Int. J. Heat Mass Transfer* **30,** 2171–2187 (1987).
29. W. D. Bennon and F. P. Incropera, The evolution of macrosegregation in statistically cast binary ingots, *Metall. Trans.* **18B,** 611–616 (1987).
30. C. Beckermann and R. Viskanta. Double-diffusive convection during dendritic solidification of a binary mixture, *PhysicoChem. Hydrodyn.* **10,** 195–213 (1988).
31. V. R. Voller, A. D. Brent and C. Prakash, The modelling of heat, mass and solute transport in solidification systems, *Int. J. Heat Mass Transfer* **32,** 1719–1732 (1989).
32. H. Shahani, G. Amberg and H. Fredriksson, On the formation of macrosegregation in unidirectionally solidified Sn–Pb and Pb–Sn alloys, *Metall. Trans.* **23A,** 2301–2311 (1992).
33. S. N. Tewari and R. Shah, Macrosegregation during steady-state arrayed growth of dendrites in directionally solidified Pb–Sn alloys, *Metall. Trans.* **23A,** 3383–3392 (1992).
34. D. G. Neilson and F. P. Incropera, Three-dimensional considerations of unidirectional solidification in a binary liquid, *Numer. Heat Transfer Pt A* **23,** 1–20 (1993).
35. D. E. J. Talbot, Effects of hydrogen in aluminium, magnesium, copper, and their alloys, *Int. Metall. Rev.* **20,** 166–184 (1975).

36. *MATLAB Users's Guide*. The Math Works Inc., Natick, MA (1992).
37. E. K. Jensen, Mathematical model calculations in level pour DC-casting of aluminium extrusion ingots. In *Light Metals* (Edited by K. J. McMinn), pp. 631–642. TMS–AIME, Warrendale, PA (1980).
38. R. D. Pehlke, A. Jeyarajan and H. Wada, Summary of thermal properties for casting alloys and mold materials, Technical Report PB83-211003, National Technical Information Service, (1983).
39. T. B. Massalski (Ed.), *Binary Alloy Phase Diagrams*, Vol. 1, 2nd Edn. ASM International (1990).
40. C. J. Smithells. *Metals Reference Book*, 5th Edn. Butterworths, London (1976).
41. L. F. Mondolfo. *Aluminium Alloys, Structure and Properties*. Butterworths, London (1976).